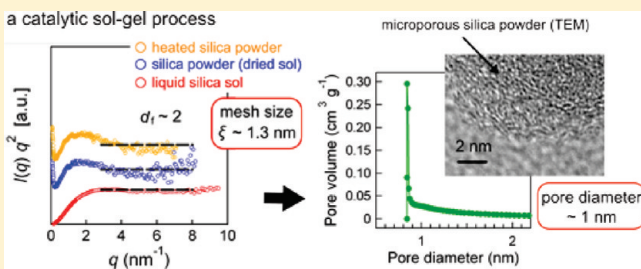


Microstructure Investigation on Micropore Formation in Microporous Silica Materials Prepared via a Catalytic Sol–Gel Process by Small Angle X–Ray Scattering

Wataru Shimizu,*† Junsuke Hokka,† Takaaki Sato,‡ Hisanao Usami,† and Yasushi Murakami†

†Division of Chemistry and Materials, Faculty of Textile Science and Technology, and ‡International Young Researchers Empowerment Center, Shinshu University, 3-15-1 Tokida, Ueda, Nagano 386-8567, Japan

ABSTRACT: The so-called sol–gel technique has been shown to be a template-free, efficient way to create functional porous silica materials having uniform micropores. This appears to be closely linked with a postulation that the formation of weakly branched polymer-like aggregates in a precursor solution is a key to the uniform micropore generation. However, how such a polymer-like structure can precisely be controlled, and further, how the generated low-fractal dimension solution structure is imprinted on the solid silica materials still remain elusive. Here we present fabrication of microporous silica from tetramethyl orthosilicate (TMOS) using a recently developed catalytic sol–gel process based on a nonionic hydroxyacetone (HA) catalyst. Small angle X-ray scattering (SAXS), nitrogen adsorption porosimetry, and transmission electron microscope (TEM) allowed us to observe the whole structural evolution, ranging from polymer-like aggregates in the precursor solution to agglomeration with heat treatment and microporous morphology of silica powders after drying and hydrolysis. Using the HA catalyst with short chain monohydric alcohols (methanol or ethanol) in the precursor solution, polymer-like aggregates having microscopic correlation length (or mesh-size) ~ 2 nm and low fractal dimensions ~ 2 , which is identical to that of an ideal coil polymer, can selectively be synthesized, yielding the uniform micropores with diameters <2 nm in the solid materials. In contrast, the absence of HA or substitution of 1-propanol led to considerably different scattering behavior reflecting the particle-like aggregate formation in the precursor solution, which resulted in the formation of mesopores (diameter >2 nm) in the solid product due to apertures between the particle-like aggregates. The data demonstrate that the extremely fine porous silica architecture comes essentially from a Gaussian polymer-like nature of the silica aggregates in the precursor having the microscopic mesh-size and their successful imprint on the solid product. The result offers a general but significantly efficient route to creating precisely designed fine porous silica materials under mild condition that serve as low refractive index and efficient thermal insulation materials in their practical applications.



1. INTRODUCTION

Porous silicon dioxide (silica) has attracted considerable attention for diverse applications owing to its fundamental character, such as chemical and thermal stability, optical transparency, and mechanical strength.^{1–3} Since nanosized pores generally contribute to the enhancement of distinctive properties of silica materials, porous silica is expected to be utilized for a wide range of functional materials, e.g., low dielectric materials,^{4–6} low refractive materials,^{2,7,8} and thermal insulators.^{9–11} Various approaches have been suggested as a pore generation technique.^{12–14} However, poor mechanical properties and performance degradation caused by penetration and adsorption of external organic substances are still inherent problems of these porous materials.^{5,15,16} Recent studies on porous materials have shown that a small pore size and its uniformity contribute to the strength.^{5,17–19} Additionally, small pores appear to prevent the deposition of chemical species in the pores.²⁰ From these standpoints, microporous silica having micropores (diameter $d < 2$ nm²¹) are highly desired

as a candidate for evolutionary materials that can overcome all of these difficulties.

When targeting the precise control of the pore size and its uniformity aimed at the silica materials that possess exclusively micropores, the geometry control of the polymer-like, low-fractal dimension structures in the precursor solution with an optimized hydrolysis/condensation reaction represents a challenge. It is established that use of a base catalyst in sol–gel process produces highly branched silica polymers, resulting in densely structured particles that easily create a void among them.²² This often leads to mesopore ($2 \text{ nm} < d < 50 \text{ nm}$) or macropore ($d > 50 \text{ nm}$) formation²¹ in the silica solids due to the fact that the void size, i.e., pore diameter, is governed by the particle geometry and size.^{22–24} On the other hand, weakly branched silica polymers characterized by a low-fractal dimension have shown to be

Received: April 11, 2011

Revised: May 13, 2011

Published: June 21, 2011

Table 1. Summary of the Preparation Process for Each of the Silica Precursor Sol and Powders^a

sample code	solvent	catalyst	chemical hydrolysis	state
LCSm	methanol	yes		liquid
LCSe	ethanol	yes		liquid
LCSp	1-propanol	yes		liquid
LSm	methanol	no		liquid
CSm ^b	methanol	yes	no	powder
CSe ^c	ethanol	yes	no	powder
HCSm	1-propanol	yes	yes	powder ^d
HCSe	methanol	yes	yes	powder ^d
HCSp	methanol	yes	yes	powder ^d
HSm	methanol	no	yes	powder ^d

^aThe powder samples were prepared by drying the liquid samples.

^bBefore the chemical hydrolysis of HCSm. ^cBefore the chemical hydrolysis of HCSe. ^dThe powders were hydrolyzed by immersing them in water at 80 °C and then dried at 40 °C.

synthesized using an acid catalyst.^{22,25–28} Micropores ($d < 2$ nm) are usually produced via an acid-catalyzed system, whereas the pore volume is not necessarily large.

Degree of branching in the precursor, which is expressed in a fractal dimension d_f , has been investigated using small-angle X-ray scattering (SAXS).²⁹ Brinker et al. obtained weakly branched silica polymers with $d_f \approx 2$ by a two step hydrolysis procedure^{22,30} of tetraethyl orthosilicate using a hydrochloric acid catalyst. Microporous structure containing small pores < 1 nm was obtained in the dried material of these silica precursor polymers. Similarly, Nair et al. used a nitric acid catalyst and suggested that the linear structure of silica precursor polymers should be appropriate for micropores formation.²⁶

Recently, we have developed a porous silica solid material having uniform micropores (diameter $<$ ca. 0.8 nm), which can be prepared via the catalytic sol–gel process using hydroxyacetone (HA) as a nonionic catalyst.³¹ The attained pore volume fraction, ca. 40%, of the microporous silica powder is higher than previously reported values. Compared with many existing approaches introducing organic templates to create micropores,^{32–38} the nonionic-catalytic sol–gel process is a simpler but more effective method requiring no template for producing microporous silica from tetramethyl orthosilicate (TMOS; $\text{Si}(\text{OCH}_3)_4$). Use of the HA catalyst enables complete removal of the residual nonionic catalyst and alkoxy groups of TMOS in a chemical hydrolysis process, in which the resultant silica solids are treated in water at 80 °C and finally produces a microporous body containing no organic compound. The microporous silica having high pore volume fraction and extremely low organic content has offered a number of noteworthy characters, such as superhydrophilicity, high transparency, a low refractive index, and a high Young's modulus.^{31,39}

We use small-angle X-ray scattering (SAXS) to investigate microstructures of the silica sols prepared using the nonionic HA catalyst. The structural evolution driven by the sol–gel reaction in the precursor solutions were pursued by time-resolved SAXS measurements for several days. The structures of the heat-treated sol and the product silica powders derived from dried sols were also investigated by SAXS and N_2 adsorption–desorption measurements. We have elucidated effects of hydrocarbon chain length of the monohydric alcohols in the solvent as well as those

of the HA catalyst on the microporous architecture of the silica solid materials.

2. EXPERIMENTAL SECTION

Materials. Tetramethyl orthosilicate (TMOS; $\text{Si}(\text{OCH}_3)_4 > 98\%$) and hydroxyacetone ($\text{CH}_3\text{COCH}_2\text{OH} > 80\%$) were purchased from Tokyo Chemical Industry, Japan. Methanol ($>99.8\%$), ethanol ($>99.5\%$), and 1-propanol ($>99.5\%$) were purchased from Wako Pure Chemical Industries, Japan. These reagents were used as received.

Synthesis. Precursor solutions were synthesized by the catalytic sol–gel process (see Table 1).^{31,39} Monohydric alcohols, e.g., methanol, ethanol, or 1-propanol, were used as solvent. TMOS, alcohol, and distilled water were mixed in a tightly closed bottle. A nonionic catalyst, hydroxyacetone, was added to each solution. A solution without the catalyst was also prepared using methanol as a control. A thoroughly mixed solution was stirred continuously and constantly at 25 °C for several days. The molar ratio of $\text{Si}(\text{OCH}_3)_4$ to H_2O was 1 to 5, and hydroxyacetone was added at an equal molar ratio to TMOS except the catalyst-free solution, resulting in the concentration of TMOS of 0.525 mol L⁻¹.

Porous silica powders were fabricated from the aged precursor solutions. The solutions, which were stirred at 25 °C for a day, were placed in a thermostatic chamber at 40 °C and then kept standing still for 3 days. The aged solutions were evaporated and dried under vacuum to produce whitish powders. The dried silica powders were hydrolyzed by immersing in water at 80 °C for 2 h to hydrolyze methoxy groups and to remove organic compounds and then dried at 40 °C for 6 h.

Small-Angle X-ray Scattering (SAXS). SAXS measurements were carried out on precursor solutions, product powders, and their model systems. A SAXSess camera (Anton Paar, Austria) attached to a sealed tube anode X-ray generator (GE Inspection Technologies, Germany) was operated at 40 kV and 50 mA. A Göbel mirror and a block collimator provide a focused monochromatic X-ray beam of $\text{Cu K}\alpha$ radiation ($\lambda = 0.1542$ nm) with a well-defined shape. A thermostatted sample holder unit (TCS 120, Anton Paar) was used to control the sample temperature at 20 °C. The two-dimensional (2D) scattering patterns recorded by an imaging-plate (IP) detector (a Cyclone, Perkin-Elmer) were integrated into one-dimensional (1D) scattered intensities, $I(q)$, as a function of the magnitude of the scattering vector $q = (4\pi/\lambda) \sin(\theta/2)$ using SAXSQuant software (Anton Paar), where θ is the total scattering angle. All the measured intensities were semiautomatically calibrated for transmission by normalizing a zero- q attenuated primary intensity to unity. All $I(q)$ data were corrected for the background scattering from the capillary and the solvents, and the absolute scale calibration was made using water as a secondary standard.⁴⁰ A model-independent collimation correction procedure was made via an indirect Fourier transformation (IFT)^{41,42} routine and/or based on a Lake algorithm. All of the fitting and fractal analyses were made after the desmeared procedure.

^{29}Si NMR. Chemical characterization of silica precursors was conducted by ^{29}Si NMR spectroscopy. All ^{29}Si spectra were obtained on an AVANCE 400 MHz FT-NMR spectrometer (Bruker, Germany) at 20 °C as a function of the reaction times at 0–48 h. All of the measurements were conducted with a pulse width of 18 μs and a pulse delay of 10 s at 79.49 MHz. Two mL of the precursor solution was put in a 10 mm NMR glass tube, and

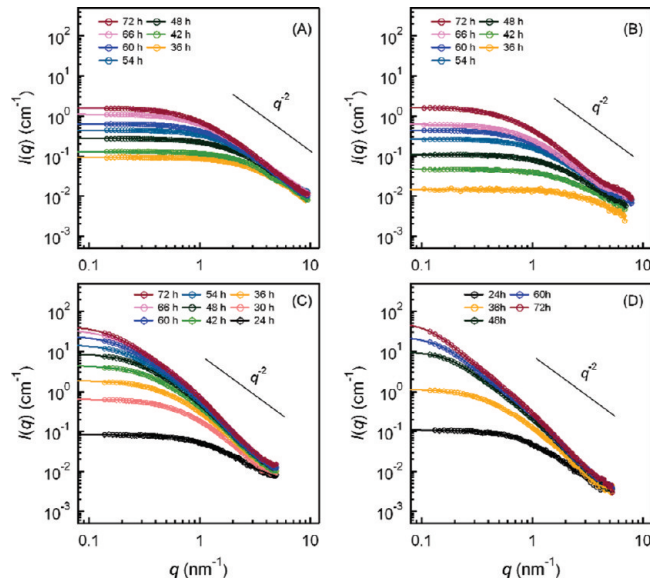


Figure 1. Variations of collimation-corrected SAXS intensities, $I(q)$, for the liquid silica precursor solutions, LCSm (A), LCSe (B), LCSp (C), and LSm (D) on absolute scale as a function of the reaction time, t , in a double-logarithmic plot. The solid lines given in all panels represent the q^{-2} slope to highlight a feature of $I(q)$ in the high- q regime.

chromium(III) acetylacetone used as a relaxation agent was well dissolved before individual measurements. All ^{29}Si chemical shifts were externally referenced to the silicon peak of hexamethyldisiloxane ($\delta = 6.68$ ppm) in a 5 mm inner tube. Spectrum peaks manifest various silicon sites in distinct chemical environments. The notation Q_i^j is commonly used to explain the degree of hydrolysis and condensation for a four functional unit (e.g., tetramethyl orthosilicate), where the subscript i and superscript j denote the number of silanols and siloxane bonds on the silicon atom, respectively. Accordingly, the number of alkoxy groups on the silicon is $4 - i - j$.

Nitrogen Adsorption Porosimetry. Nitrogen gas adsorption–desorption isotherms were performed at $-196\text{ }^\circ\text{C}$ on an ASAP2010 volumetric adsorption analyzer (Micromeritics), after the heated powders were outgassed under vacuum at $200\text{ }^\circ\text{C}$ in the degassing port. Specific pore volume and surface area of the micropores were evaluated from the adsorption isotherm data using the t -plot method^{38,44} in the thickness range of $0.35\text{--}0.5$ nm, an empirical method based on the comparison of the obtained nitrogen adsorption isotherm for a porous sample with that of a nonporous reference material. A plot of the adsorption volume versus the statistical thickness of adsorbed layer on a reference surface was used in the t -plot method. Specific surface area was also calculated from the data in the relative pressure range from 0.05 to 0.3 using Brunauer–Emmett–Teller (BET) method,⁴⁶ and total pore volumes were determined from the volume of the adsorbed nitrogen gas at a relative pressure of 0.95.²¹ The pore size distributions in the pore diameter in the range of $2\text{--}10$ nm were evaluated by the Barrett–Joyner–Halenda (BJH) method,⁴⁷ whereas those of <2 nm were measured by the Saito–Foley (SF) modified Horváth–Kawazoe (HK) model from the adsorption isotherms in the low relative pressure region.^{48,49}

Transmission Electron Microscope (TEM) Observation. TEM images of the powder samples were obtained using a

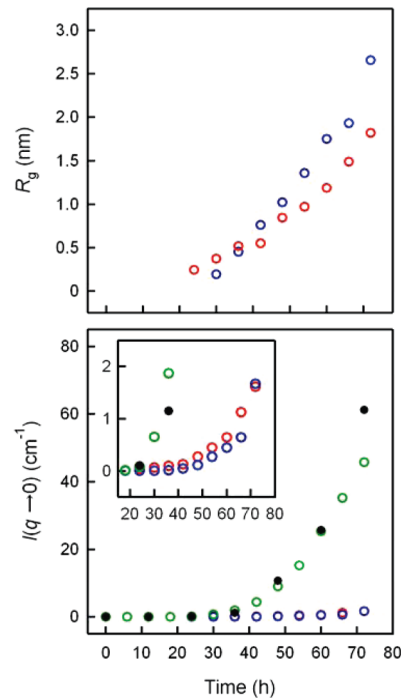


Figure 2. Extrapolated forward intensities to zero scattering vector, $I(q \rightarrow 0)$, of LCSm (red), LCSe (blue), LCSp (green), and LSm (black) plotted against the reaction time. The radius of gyration, R_g , for LCSm and LCSe determined with Guinier plot are also plotted in the upper panel. The inset shows an enlarged view of the low intensity regime for LCSm, LCSe, and LCSp, where $I(q \rightarrow 0) < 2\text{ cm}^{-1}$.

JEM-2010 transmission electron microscope (JEOL, Japan) with an acceleration voltage of 200 kV. Fine ground powders were dispersed in methanol by ultrasonication. One drop of the suspensions was put on a 150 mesh carbon-coated copper grid, and then they were dried at $60\text{ }^\circ\text{C}$ in air.

3. RESULTS AND DISCUSSIONS

3.1. Structure Characterization of the Precursor Solutions As Obtained by SAXS. It is postulated that the porous structure of the sol–gel derived solid materials reflects the conformation of the aggregates in the liquid precursors.^{22,26,30} We have evaluated the time evolution of static structures in the silica precursor solutions by means of SAXS.⁵⁰ Figure 1 shows SAXS experiments on the silica precursor solutions prepared using different monohydric alcohols with and without the HA catalyst, in which collimation–corrected SAXS intensities, $I(q)$, for LCSm, LCSe, LCSp, and LSm are given in a double-logarithmic plot as a function of the reaction time, t .

The pronounced increase of $I(q)$ with time for all of the systems with reaction time provides evidence for the growth of the silica aggregates in the precursor solutions. In Figure 2, we display the extrapolated forward intensities to zero scattering vector, $I(q \rightarrow 0)$, of all the precursor solutions together with the radius of gyration, R_g , of LCSm and LCSe (R_g of LCSp and LSm are not accessible because Guinier regime $qR_g < 1$ for these samples was beyond the resolution of our SAXS experiments). Importantly, we found that, independent of hydrocarbon chain lengths of the solvent alcohols and of the presence or absence of the HA catalyst, all of the precursor solutions showed induction

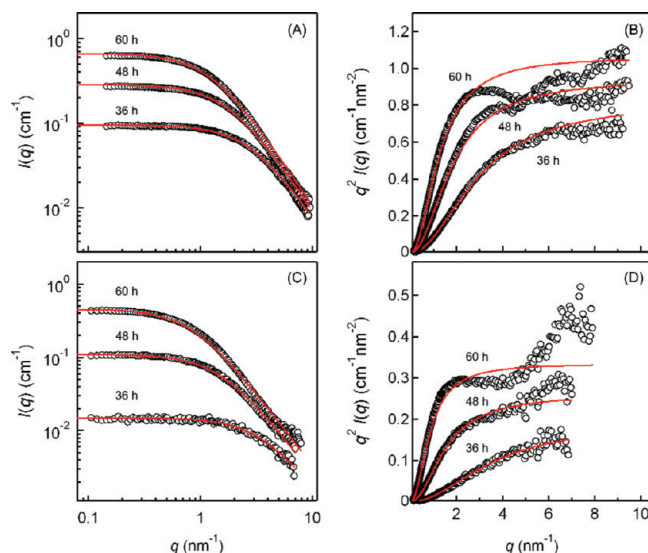


Figure 3. Collimation-corrected SAXS intensities, $I(q)$, and Kratky plots, $q^2 I(q)$ versus q , of the methanol- and ethanol-based precursor solutions with the HA catalyst, forming low-fractal dimension polymer-like aggregates with $d_f \approx 2$; LCSm (A and B) and LCSe (C and D), as a function of the reaction time at 36, 48, and 60 h. Red solid lines represent the optimum fit curves based on Ornstein–Zernike (OZ) equation.

times for an increase of $I(q \rightarrow 0)$. The SAXS intensity should remain nearly constant until the size of silica aggregates and their number density are large enough to scatter X-rays to be detected, so that the observed induction times are likely to involve the induction time for nucleation, the actual nucleation period, and the period for the aggregate growth up to a certain size that can clearly be detected by SAXS experiments.

The onset of the intensity rise for the methanol- and ethanol-based systems with the HA catalysts, i.e., LCSm and LCSe, was found to be ca. 36 h. The polymerization in these systems proceeded slowly at $t > 36$ h, yielding the relatively small molecular weights even after 3 days. In contrast, when 1-propanol was substituted for methanol or ethanol (LCSp), we observed the earlier onset (ca. 24 h). The aggregates exhibited far faster growth than those observed in LCSm and LCSe in $t > 24$ h, and finally reached several tens of times greater relative intensities than those for LCSm and LCSe. The absence of the HA catalyst (LSm) also led to faster growth and high molecular weights of the aggregates, similar to the behavior of the 1-propanol-based LCSp. We infer that for the induction periods, hydrolyzed species may have been created by the hydrolysis reaction of TMOS that serves as a polymerization nucleus of the following condensation reaction, but polycondensation did not proceed actively.

3.2. Scattering Functions of the Precursor Solutions LCSm and LCSe. For further quantitative description of the silica aggregate structure in the precursor solutions, we scrutinized the shape of the scattering curves. We found that when methanol or ethanol was used with the HA catalyst in the precursor solutions, namely for LCSm and LCSe, $I(q)$ can formally be fitted by the Ornstein–Zernike (OZ) equation⁵¹

$$I(q) = \frac{I(0)}{1 + \xi^2 q^2} \quad (1)$$

where ξ is the correlation length and $I(0)$ the asymptotic zero- q intensity. In Figure 3, SAXS intensities, $I(q)$, and Kratky plots,

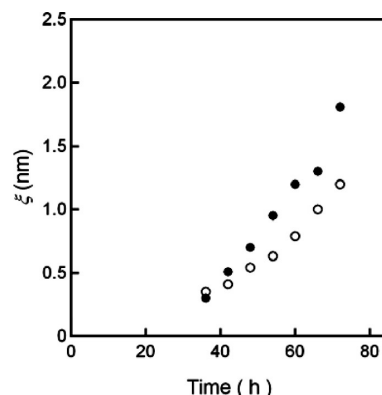


Figure 4. Variation of the correlation length (mesh-size), ξ , of LCSm (open circle) and LCSe (filled circle) with the reaction time.

$q^2 I(q)$ versus q , of LCSm and LCSe are displayed. Note that the shape of the OZ function is not the same as, but resembles that of the Debye structure function, $P_{\text{ideal}}(q)$, of an ideal or Gaussian polymer chain in solution^{52–54}

$$I(q) = I(0)P_{\text{ideal}}(u) = 2I(0) \frac{\exp(-u) + u - 1}{u^2} \quad (2)$$

where $u = R_g^2 q^2$ with R_g being the radius of gyration.

At low- q , $I(q)$ exhibited Guinier behavior reflecting the overall geometry of the aggregates, as described by a Guinier equation

$$I(q) = I(0) \exp \left[-\frac{R_g^2 q^2}{3} \right] \quad (3)$$

In the intermediate to high- q regime, power-law behavior was observed, indicating the emergence of the fractal structures. Self-similarity is an important basic property of fractal objects like polymer chains in solution, which means that independent of the chosen length scale, a polymer chain exhibits the identical internal structure.⁵⁵ The number of monomers, $n(r)$, contained in a sphere of radius r is represented by the following power law with an exponent ν :

$$n(r) \propto r^\nu \quad (4)$$

The fractal dimension, d_f , is just defined as the above-mentioned exponent ν , where $\nu = 2$ corresponds to an ideal coil polymer without excluded volume, while $\nu = 5/3$ to an expanded chain with excluded volume in good solvent. d_f directly shows up in the asymptotic exponent in $I(q)$ as

$$I(q) \propto q^{-d_f} \quad (5)$$

The q^{-2} slope in $I(q)$ observed for LCSm and LCSe at $q > 2$ nm $^{-1}$ gives $d_f \approx 2$, which is identical with d_f of an ideal polymer chain. A Kratky plot, $q^2 I(q)$ versus q , is an instructive way to highlight a fractal nature with $d_f \approx 2$, which is manifested in the high- q plateau ($q^2 I(q) \propto q^0$). The finding demonstrates that low fractal dimension, polymer-like aggregates were synthesized by using the HA catalyst with short-chain alcohols, methanol and ethanol. The local stiffness of a polymer chain often leads to rod-like properties on a short length scale, which is revealed in the highest- q regime of SAXS curve. The position of crossover, q^* , from coil-like [$I(q) \propto q^{-2}$] to rod-like scattering [$I(q) \propto q^{-1}$], can clearly and only vaguely be seen for LCSe and LCSm,

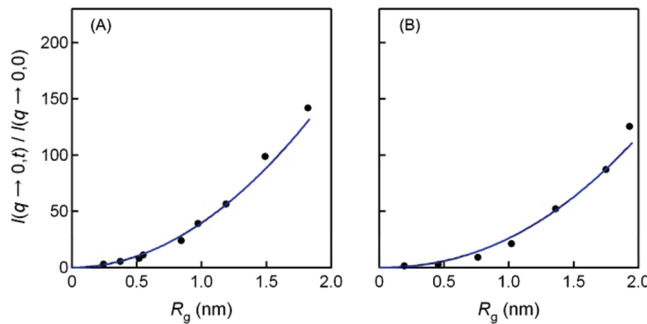


Figure 5. Relative forward intensity, $I(q \rightarrow 0, t)/I(q \rightarrow 0, 0)$, versus the radius of gyration, R_g for LCSm (A) and LCSe (B). $I(q \rightarrow 0, t)/I(q \rightarrow 0, 0)$ may be used as a measure of the weight-averaged apparent molecular weight, M_w^{app} , of the polymer-like aggregates. Solid lines are the optimum fit curves drawn under the assumption of $M_w^{app} \propto R_g^\nu$, yielding $\nu = 1.98$ and 2.17 for LCSm and LCSe, respectively.

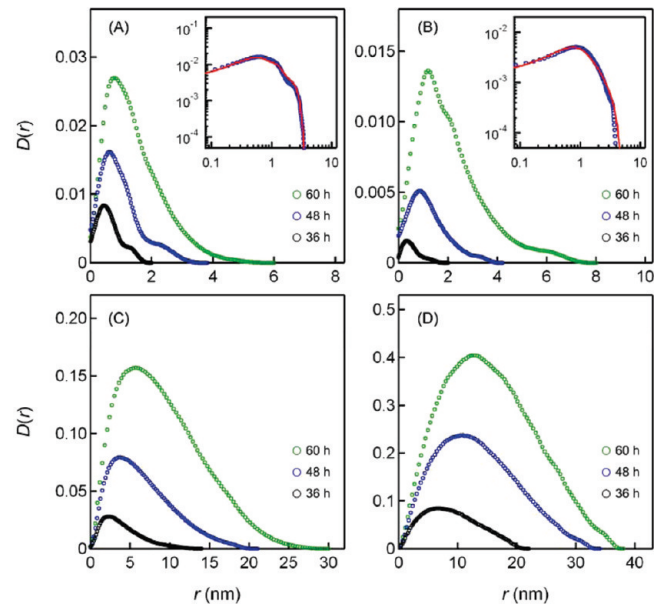


Figure 7. Monomer–monomer pair correlation functions in the expression of $D(r) = \langle c_m \rangle [g(r) - 1]r^2$ for LCSm (A), LCSe (B), LCSp (C), and LSm (D) after 36, 48, and 60 h. In the insets of (A) and (B), shown is the comparison of the experimentally obtained $D(r)$ with that for the OZ function, $D(r) = \langle c_m \rangle [\exp(-\xi/r)/r]^2$.

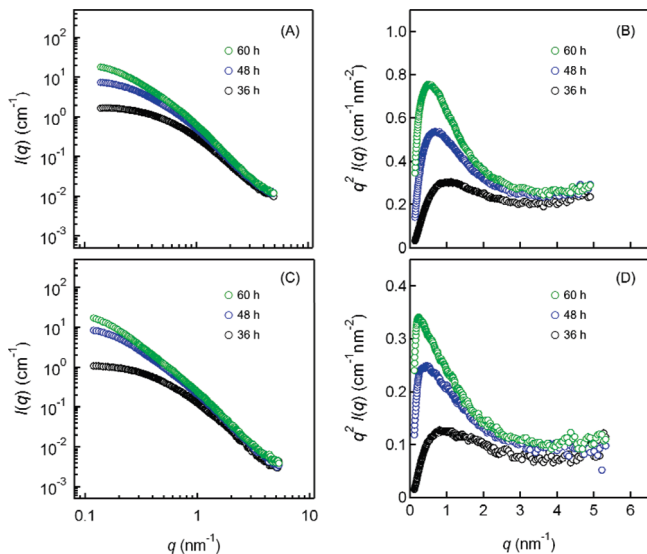


Figure 6. Typical SAXS intensities, $I(q)$, and Kratky plots, $q^2 I(q)$ versus q , of the 1-propanol-based precursor solutions with the HA catalyst, LCSp (A and B), and the methanol-based precursor solutions without the HA catalyst, LSm (C and D), forming branched polymer-like or particle-like aggregates as a function of the reaction time at 36, 48, and 60 h.

respectively, which corresponds to persistence length, $l_{ps} \approx \pi/q^*$; see Figure 3, panels B and D.

The correlation length, ξ , explicitly involved in the OZ expression (eq 1) can be interpreted as the mesh-size of the transient polymer network,⁵⁴ representing the length scale of the spatial correlation of density fluctuations caused by a polymer chain.⁵⁵ Figure 4 shows variation of ξ in the methanol-based and ethanol-based precursor solutions with the HA catalyst as a function of the reaction time as obtained by SAXS. We observed that ξ was an increasing function of time, LCSm showing greater values than LCSe. Importantly, even after 3 days, the growth of ξ was rather limited; LCSm gave $\xi \sim 1.3 \text{ nm}$ at $t = 72 \text{ h}$, while LCSe did $\xi \sim 1.9 \text{ nm}$. As we will discuss in the following sections, such geometry found in the liquid precursors is closely linked with the pore size of the resulting solid silica materials produced from LCSm and LCSe.

Generally, the asymptotic zero- q intensity, $I(q \rightarrow 0)$, gives a measure of molecular weight of a polymer chain in a dilute solution. This relation is no longer exact for a semidilute solution because osmotic compressibility also contributes to $I(q \rightarrow 0)$.^{53–55} Nevertheless, the apparent (relative) molecular weight, M_w^{app} , of the polymer-like aggregates in the precursor solutions may be semiquantitatively evaluated, relying on the relative forward intensity, $I(q \rightarrow 0, t)/I(q \rightarrow 0, 0)$. In Figure 5, we show $I(q \rightarrow 0, t)/I(q \rightarrow 0, 0)$ plotted against R_g evaluated based on eq 3 using a Guinier plot [$\ln I(q)$ vs q^2]. With increasing R_g , $I(q \rightarrow 0, t)/I(q \rightarrow 0, 0)$ increased, showing downward convex behavior, in which interplay of mass and the extent of spatial distribution of a polymer-like aggregate is manifested; solid lines are the optimum fit curves under the assumption of $M_w^{app} \propto R_g^\nu$. These exponents were evaluated as $\nu = 1.98$ and 2.17 for LCSm and LCSe, respectively. The exponent of ca. 2 again confirms the growth of the weakly branched coil polymer-like aggregates.

All the data presented in Figures 3–5 unambiguously demonstrate that Gaussian polymer-like aggregates having microscopic correlation length (or mesh-size) $< 2 \text{ nm}$ and low fractal dimensions ~ 2 , can selectively be synthesized in the precursor solutions based on a short chain alcohol (methanol or ethanol) and the HA catalysts.

3.3. Scattering Behavior of the LCSp and LSm Precursor Solutions. We also investigated the precursor solutions based on 1-propanol (LCSp) and without the HA catalyst (LSm). As we discuss later, these precursor solutions resulted in the mesopore formation. In Figure 6, we present SAXS intensities, $I(q)$, and Kratky plots, $q^2 I(q)$ versus q , of LCSp and LSm. Figure 6 indicates that in contrast to the observation that the weakly branched polymer-like aggregates in LCSm and LCSe exhibited very similar behavior to an ideal polymer chains, substitution of 1-propanol or the absence of the HA catalyst led to considerably

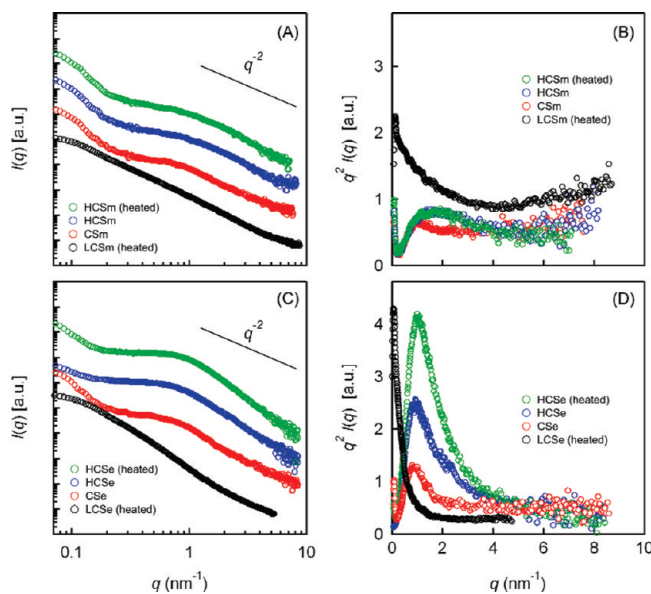


Figure 8. SAXS intensities, $I(q)$, and a Kratky plot, $q^2I(q)$, of the heat-treated sol and the silica powder samples synthesized from the methanol-based (A and B) and the ethanol-based (C and D) precursor solutions. $I(q)$ and $q^2I(q)$ for heat-treated sol from LCSm (black), CSm (red), HCSm (blue), and HCSm heated at 200 °C (green) are shown in the panels (A) and (B), respectively, and those for heat-treated sol from LCSe (black), CSe (red), HCSe (blue), and HCSe after the same heat treatment (green) in the panels (C) and (D).

different scattering behavior. $I(q)$ for LSCp and LSm cannot be described by the OZ function, representing a local maximum in the Kratky plot. It is naturally understood that branching of polymer chains imposes a somewhat particle-like nature to the polymer chains. Toporowski and Roovers predicted that star-branched polymers give such a local maximum in a Kratky plot.⁵³ Similar phenomenon was observed for dendrimers⁵⁷ and nanoparticles comprising tightly cross-linked linear chain precursors.⁵⁵ If a Kratky plot is applied to hardsphere, it gives a low- q local maximum and the rapid decrease at high- q as $q^2I(q) \propto q^{-2}$. However, unlike the expected behavior for a colloidal particle having homogeneous density, a high- q plateau after a local maximum is still present for LSCp and LSm. We suggest that such notable features of in LSCp and LSm are due to the coexisting particle-like and Gaussian chain-like natures of the branched polymer-like aggregates in these systems.

The shape of the scattering function for a polymer is governed by the structure function, $S_{poly}(q)$, which is given by Fourier transformation of the monomer–monomer pair-correlation function, $g(r)$

$$I(q) \propto S_{poly}(q) = 4\pi\langle c_m \rangle \int_0^\infty [g(r) - 1] r^2 \frac{\sin qr}{qr} dr \quad (6)$$

where $\langle c_m \rangle$ is averaged monomer concentration. For a dilute solution, $g(r)$ describes the correlations within a single chain, whereas for a semidilute solution, $g(r)$ inevitably involves those between different chains. Using indirect Fourier transformation (IFT) technique,^{40,41} we deduced $g(r)$. Figure 7 shows the monomer–monomer pair correlation functions of the silica precursors, LCSm, LCSe, LSCp, and LSm, in the expression of $D(r) = \langle c_m \rangle [g(r) - 1] r^2$. This expression provides intuitive information about the extent of spatial distribution of the

polymer-like silica aggregates. As shown in the insets of Figure 7, $D(r)$ of LSCm (TMOS/methanol/water/HA) and LCSe (TMOS/ethanol/water/HA) are well explained by that of an ideal polymer. However, obviously, $D(r)$ of LSCp (TMOS/1-porpanol/water/HA) and LSm (TMOS/water/methanol) cannot be described by $D(r)$ of an ideal linear polymer.

According to the definitions and formulations, $D(r)$ for the branched polymer-like aggregates, as detected in LSCp and LSm, may be understood as a counterpart of the pair-distance distribution function, $p(r)$, of a colloidal dispersion, which is given by the convolution square of the electron density fluctuations, $\Delta\rho(r)$

$$p(r) \equiv \Delta\tilde{\rho}^2(r)r^2 = \left\langle \int_{-\infty}^{\infty} \Delta\rho(r_1)\Delta\rho(r_1 - r) dr_1 \right\rangle r^2 \quad (7)$$

For a dilute colloidal dispersion, the intensity $I(q)$ is given by

$$I(q) \sim P(q) = 4\pi \int_0^\infty p(r) \frac{\sin qr}{qr} dr \quad (8)$$

where $P(q)$ is form factor of a colloidal particle.^{40,41,58,59} Indeed, $D(r)$ of LSCp and LSm looks more like $p(r)$ of to some extent elongated colloidal dispersions, which underlines the different structural aspects of LSCp and LSm from those of LCSm and LCSe.

3.4. Fractal Structure of the Solid Silica Powders. The microstructure of the liquid silica precursors should be a key factor that affects the structure of the dried silica powder products. How the liquid precursor structures is ‘imprinted’ on the solid silica materials is of our especial interest. In Figure 8, we show SAXS intensities, $I(q)$, and Kratky plots, $q^2I(q)$ versus q , of the silica powders derived from the LCSm and LCSe precursor solutions, together with those of heat-treated sols. Different from the typical scattering pattern of the liquid precursors, the powder samples exhibited multiasymptotic behavior of $I(q)$, which is probably caused by polymer–polymer agglomeration via the heat treatment and drying process. Importantly, the SAXS data revealed that a series of the methanol-based treated samples, e.g., the heat-treated LCSm sol, the silica powder produced by drying the heat-treated sol at 40 °C (CSm), the hydrolyzed silica powder (HCSm), and the heat-treated HCSm powder at 200 °C, commonly exhibited the plateau in their Kratky plot in $q > \sim 2 \text{ nm}^{-1}$. This means the constant monomer density was achieved on a small length scale corresponding to $q > \sim 2 \text{ nm}^{-1}$, while large length-scale structures were modified via the heat and hydrolysis treatments. The finding is highly indicative of the preserved fractal nature in the internal (local) structures of the hydrolyzed and heat-treated silica powders, i.e., $d_f \approx 2$ and $\xi < 2 \text{ nm}$, found in the liquid precursor.

As for the silica powders fabricated from LCSe, the q -position where $q^2I(q)$ reaches a plateau shifted to higher- q side with a series of the treatments, which appears to suggest an increasing mesh-size. The HCSe and the heat-treated HCSe powder sample showed a negative slope in their Kratky plots ($d_f > 2$), indicating that additional cross-linking reactions via the hydrolysis and heat treatments caused the emergence of higher fractal-dimension structures. With respect to this observation, it is said that the porous structures derived from LCSe with larger geometry than those from LCSm are relatively fragile against the chemical reactions.

3.5. ^{29}Si NMR Investigation of Weakly Branched Silica polymers. The degree of hydrolysis of a silicon alkoxide monomer is

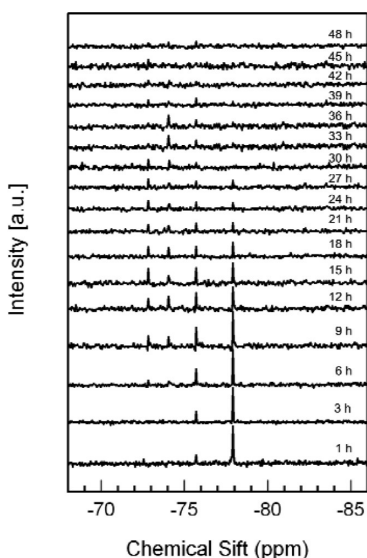


Figure 9. Time evolution of the hydrolysis reaction in the methanol-based precursor solution under the presence of the HA catalyst as obtained by ^{29}Si NMR spectroscopy. A time series (from bottom to top) of the ^{29}Si NMR spectra for LCSm as a function of the reaction time, t .

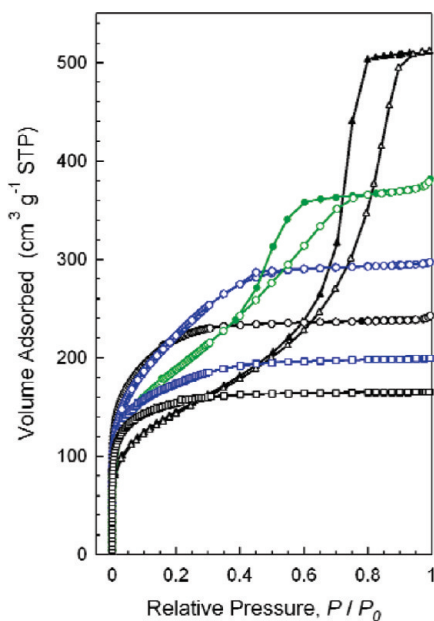


Figure 10. Nitrogen adsorption–desorption isotherms of the hydrolyzed silica powders prepared from the HA catalyst-involved precursor solutions with different monohydric alcohols; HCSm (black circle), HCSe (blue circle), and HCSp (green circle), and that from the methanol-based precursor without the HA catalyst; HSm (black triangle). The data for the powders without the hydrolysis treatment, CSm (black square) and CSe (blue square), are also compared in the plot. All samples were heat-treated at $200\text{ }^\circ\text{C}$ for 6 h to degas. The adsorption and desorption isotherms are represented by open and filled symbols, respectively.

considered as one of the influencing factors for the generation of weakly branched Gaussian chain-like polymers. In order to confirm the state variations of Si sites by the hydrolysis and condensation reactions, we conducted a ^{29}Si NMR experiment

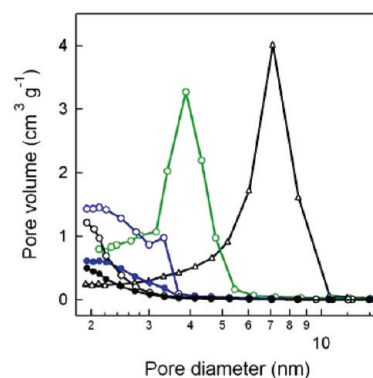


Figure 11. BJH pore size distributions of the hydrolyzed silica powders, HCSm (black open circles), HCSe (blue open circles), HCSp (green open circles), and HSm (open triangles). For comparison, the data for the powders without the hydrolysis treatment, CSm (black filled circle) and CSe (blue filled circle), are also displayed.

on the methanol-based precursor solutions with the HA catalysts (LCSm) in an early stage of the sol–gel process (Figure 9). ^{29}Si NMR spectra were recorded at $1 \leq t/\text{h} \leq 48$, where t is the reaction time. A Q_0^1 peak intensity at -75.6 ppm increased with the reaction time in $t < 9\text{ h}$, whereas a Q_0^0 peak intensity at -77.9 ppm decreased. Q_0^2 and Q_0^3 peaks appeared respectively at -74.0 and -72.8 ppm at $t \sim 6\text{ h}$. The Q_0^2 peak exhibited the maximum area at $t \sim 12\text{ h}$, which was smaller than that of Q_0^3 . The maximum area of the Q_0^3 peak was attained at $t \sim 15\text{ h}$. The Q_0^3 peak is the larger than any other Q_0 peak after the 24-h reaction. No Q_0^4 peak was observed, which was expected to appear at about -73.1 ppm .^{22,60}

A total intensity of the Q_0^0 , Q_0^1 , Q_0^2 , and Q_0^3 peaks was reduced with reaction time. This implies an increase in the number of condensed sites (e.g., Q_1) produced by the condensation reaction of hydrolyzed silicon monomers, while the peaks attributed to Q_1 sites were hidden in a background because of their blurred signals. The consumption of Si monomers was almost completed in $t < 48\text{ h}$, in which the condensation reaction between partially hydrolyzed silicon sites proceeded. The data demonstrate that although a sufficient amount of water was added to the solution ($[\text{TMOS}]:[\text{H}_2\text{O}] = 5$), a fully hydrolyzed site Q_0^4 was not generated. This notable feature well supports the SAXS results; the condensation of partially hydrolyzed silicon sites efficiently suppressed the branch formation, leading to the weakly branched polymer-like structure. In contrast, an ionic catalyst, e.g., hydrochloride,^{60–62} generally leads a rapid hydrolysis reaction, producing completely hydrolyzed silicon site Q_0^4 .²² Such fully hydrolyzed silicon atoms often enhance the branch formation, yielding particle-like highly branched aggregates.²²

3.6. Pore Characteristic of the Produced Silica Powders. In order to determine the pore characters of the silica powder samples, we conducted the N_2 adsorption–desorption measurements on CSm, HCSm, CSe, and HCSe. The hydrolyzed powders, HCSp and HSm, derived from the LCSp and LSm precursor solutions, respectively, were also evaluated. A N_2 adsorption–desorption isotherm obtained for HCSm, CSm, and CSe showed a typical type I isotherm (Figure 10). According to IUPAC, this is classified into monolayer adsorption of N_2 ,²¹ which represents a porous material based on micropores in diameter $< 2\text{ nm}$. The N_2 adsorption–desorption isotherm of

Table 2. Structural Properties of the Porous Silica Samples ^a

sample code	<i>d</i> (nm)	<i>S</i> _{micro} (m ² g ⁻¹)	<i>S</i> _{total} (m ² g ⁻¹)	<i>V</i> _{micro} (m ³ g ⁻¹)	<i>V</i> _{total} (m ³ g ⁻¹)
CSm	<2.0	295	515	0.141	0.26
CSe	2.1	257	588	0.122	0.31
HCSm	<2.0	260	737	0.125	0.37
HCSe	2.8	6	780	0.004	0.46
HCSp	3.5	31	660	0.016	0.58
HSm	6.1	68	517	0.024	0.79

^a Notation: *d*, average pore diameter (BET); *S*_{micro}, micropore surface area; *S*_{total}, total surface area (BET); *V*_{micro}, micropore volume; *V*_{total}, total pore volume.

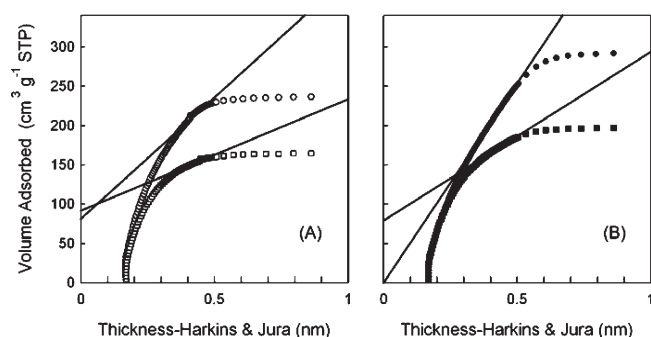


Figure 12. Effects of chemical hydrolysis on the micropore volume of the solid silica materials. *t*-plot curves of the silica powder samples; (A) the methanol-based systems, HCSm (open circle) and CSm (open square), and (B) the ethanol-based systems, HCSe (filled circle) and CSe (filled square). Tangent lines were drawn in the thickness range between 0.35 and 0.5 nm.

HCSe showed a type I isotherm with minor hysteresis loops, whereas those of HCSp and HSm showed typically type IV isotherms. The minor hysteresis loop of HCSe indicates the presence of pores having slightly larger pore diameter than that of the micropore. The hysteresis loop of HCSp fell into a H2 type associated with an ink bottle shape of pores.²¹ In contrast, HSm, derived from the methanol-based precursor solution without HA catalyst (LSm) showed a H1 type hysteresis loop, which implies an aggregate as an assembly of particles. The result is consistent with the SAXS data which have shown the formation of branched polymer-like or somewhat particle-like silica aggregates in the LCSp and LSm precursor solutions.

In Figure 11, we show the BJH pore size distributions for a series of hydrolyzed silica powders calculated from the N₂ adsorption data. CSm and HCSm exhibited no obvious peak in the range from 2 to 10 nm. The distributions marked in the vicinity of *d* ~ 2 nm appear to reflect the amount of micropores. The total pore volumes of CSm and HCSm were estimated to be 0.26 and 0.37 cm³ g⁻¹, respectively (Table 2). An increase of the pore volume by the chemical hydrolysis treatment was also observed in our previous studies.^{31,39} One plausible reason for this phenomenon is that chemical substances remaining in the solid matrix were eliminated by the chemical hydrolysis. A broad shoulder can be seen in the pore size distribution of CSe in the range of 2 ≤ *d*/nm ≤ 4. After the hydrolysis (HCSe), a small peak at 3.3 nm emerged in the broad distribution. The total pore volume of 0.31 and 0.46 cm³ g⁻¹ were obtained for CSe and

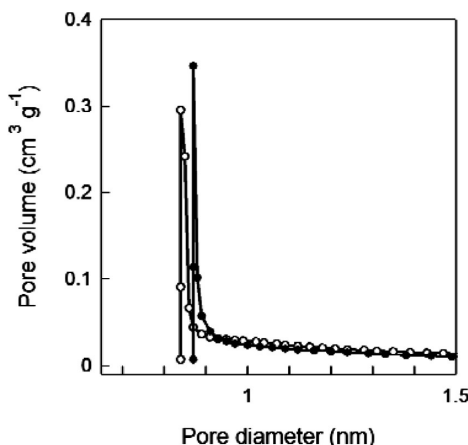


Figure 13. SF-modified HK pore size distributions for the microporous silica, HCSm (open circle) and CSm (filled circle).

HCSe, respectively (Table 2). In the ethanol-based powders, aside from the targeted elimination of the remains of chemicals, the hydrolysis caused an increase of large-sized pores (*d* ~ 3.3 nm). On the one hand, the pore size distributions of HCSp and HSm, which were produced from the branched polymer-like or particle-like silica aggregates, showed distinct peaks at 3.9 and 7.1 nm, respectively, highly indicative of the mesopore formation.

The *t*-plot analysis, commonly used to determine the micropore volume of microporous materials, was applied to CSm, HCSm, CSe, and HCSe to confirm the presence of micropores. The *t*-plots of CSm and HCSm are given in Figure 12A. Extrapolation lines for CSm and HCSm determined in the thickness range between 0.35 and 0.5 nm had a positive intercept on the *y*-axis, indicating the presence of micropores. In addition, the values of their *y*-intercept were close to each other. This means that the micropore structure was preserved after the chemical hydrolysis, owing to the robust micropore architecture. In view of the SAXS results shown in Figure 8, panels A and B, these powders are characterized by *d*_f ≈ 2 in their local structures. All of these observations led us to conclude that the weakly branched polymer-like structure in the liquid precursor offers a micropore framework of the resulting solid silica, whose pore size is regulated by the mesh-size (ξ) of the transient polymer network produced in the precursor solutions. These samples did not generate secondary pores, which are usually formed in the aggregate of grown polymers during the drying process.²² We infer that mutual interpenetration of the weakly branched silica aggregates generated in the liquid precursor, known as an important nature of Gaussian polymer chains, efficiently avoided the secondary pore creation via the drying process.

To scrutinize the pore size distribution in the micropore region of *d* < 2, we applied the SF modified HK model⁴⁸ to CSm and HCSm. This approach is based on a semiempirical calculation of the pore size distribution from the nitrogen adsorption isotherm in microporous materials with slit-like pores, and is applicable to active carbon. Its application was extended to the cylindrical pore geometry of microporous materials, such as zeolite and silica,⁴⁹ and have been used in many studies on microporous silica.^{63,64}

We found that CSm and HCSm exhibited narrow peaks at 0.87 and 0.84 nm, respectively (Figure 13). After the hydrolysis treatment, the micropore diameters only slightly decreased. The residual methoxy groups in the polymeric precursors may

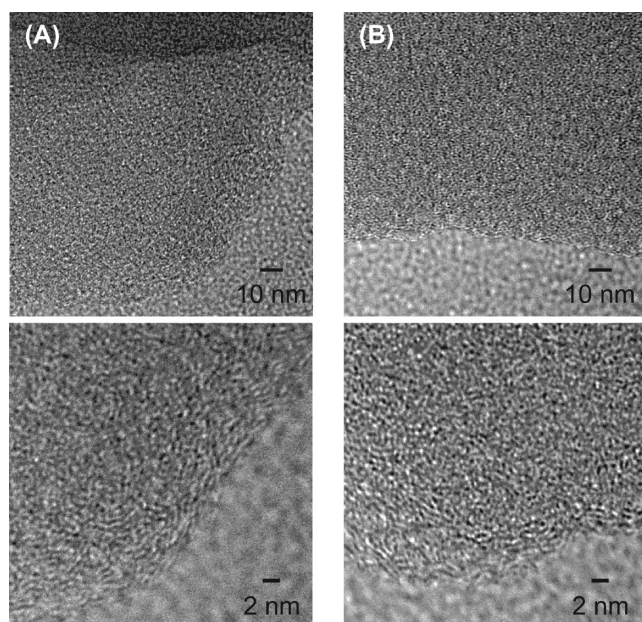


Figure 14. Typical TEM images of the dried silica powders, CSm (A) and the heated HCSm (B).

have been hydrolyzed and converted to silanol groups. The porous silica powders derived from the ethanol system, CSe, had a certainly larger average pore diameter than those derived from the methanol systems, CSm and HCSm (Table 2). The finding again demonstrates that the micropore size of silica solid materials was linked with the mesh-size (ξ) of the polymeric silica precursors (Figure 4).

We postulate that the larger pore size of the silica powder from the ethanol system (CSe) enhanced incorporation of water molecules in the hydrolysis process than that from the methanol system (CSm), which expanded the pore size (HCSe). As shown in Figure 11, CSe and HCSe exhibited wider pore-size distribution compared with CSm; secondary pores may seem to have been included in some degree. For the 1-propanol system (HCSp) or the catalyst-free system (HSm), the majority was mesopores caused by the cluster aggregation. Secondary pore structures are generally fragile against hydrolysis and polycondensation reactions in hydrothermal treatment.

The morphologies of CSm and HCSm were observed by TEM to obtain insights into the influence of the hydrolysis treatment on the porous structures (Figure 14). The comparison of these images confirmed almost the same morphologies in CSm and HCSm. The pore diameters of both CSm and HCSm were estimated to be ca. 0.5 nm.

■ CONCLUSION

Microporous silica solids have successfully been synthesized from TMOS via the catalytic sol–gel process using the nonionic HA catalyst. In the presence of HA, the pore size can essentially be controlled in terms of the chain length of the monohydric alcohols used in the precursor solutions, as $d < 1$ nm was attained with LCSm (TMOS/methanol/water/HA). SAXS experiments have revealed that, in the methanol- and ethanol-based systems, the polymer-like silica aggregates characterized by low fractal dimensions, $d_f \approx 2$, identical to an ideal polymer chain, and the microscopic mesh-size of the transient polymer network

($\xi < 2$ nm) were generated via the condensation of partially hydrolyzed silicon alkoxides, which offered a micropore framework of the silica solids. The agglomerated sol by the heat treatment and the solid silica powders derived from LSCm also exhibited fractal scattering behavior on a similar length scale to that in LCSm. The finding is indicative of the preserved fractal nature in their internal structures, i.e., $d_f \approx 2$ and $\xi < 2$ nm. The average pore diameter of the silica powders derived from the ethanol system (LCSe) increased via the chemical hydrolysis treatment from 2.1 to 2.8 nm, accompanied by an increase in the fractal dimension ($d_f > 2$). The phenomena highlight the advantage of the robust porous architecture of the methanol-based system against the chemical hydrolysis treatment owing to the ultrafine liquid ($\xi \sim 1$ nm) and solid ($d < 1$ nm) structures. Substitution of 1-propanol or the absence of the HA catalyst led to higher dimension branched polymers or particle-like structures in the liquid precursors, which resulted in the formation of mesopores with a diameter (>2 nm) due to apertures between the particle-like aggregates.

The data demonstrate that our unique synthetic strategy enables us to control the micropores size, simultaneously suppressing the mesopore formation. Obviously, such a scenario underlines the cardinal importance of the fine control of the liquid precursor structures to achieve the desired porosity of the solid silica materials. Our results would offer helpful guidance for fabricating extremely fine porous silica materials toward their practical applications.

■ AUTHOR INFORMATION

Corresponding Author

*Phone +81-268-21-5469. Fax +81-268-21-5447. E-mail wats@shinshu-u.ac.jp.

■ ACKNOWLEDGMENT

This work was supported by CLUSTER (the second stage) of the Ministry of Education, Culture, Sports, Science and Technology, Japan.

■ REFERENCES

- Falcaro, P.; Grosso, D.; Amenitsch, H.; Innocenzi, P. *J. Phys. Chem. B* **2004**, *108*, 10942–10948.
- Vincent, A.; Babu, S.; Brinley, E.; Karakoti, A.; Deshpande, S.; Seal, S. *J. Phys. Chem. C* **2007**, *111*, 8291–8298.
- Hoshikawa, Y.; Yabe, H.; Nomura, A.; Yamaki, T.; Shimojima, A.; Okubo, T. *Chem. Mater.* **2010**, *22*, 12–14.
- Jain, A.; Rogojevic, S.; Ponoth, S.; Agarwal, N.; Matthew, I.; Gill, W. M.; Persans, P.; Tomozawa, M.; Plawsky, J. L.; Simonyi, E. *Thin Solid Films* **2001**, *398*, 513–522.
- Hatton, B. D.; Landskron, K.; Hunks, W. J.; Bennett, M. R.; Shukaris, D.; Perovic, D. D.; Ozin, G. A. *Mater. Today* **2006**, *9*, 22–31.
- Wang, W. D.; Grozea, D.; Kim, A.; Perovic, D. D.; Ozin, G. A. *Adv. Mater.* **2010**, *22*, 99.
- Thomas, I. M. *Appl. Opt.* **1992**, *31*, 6145–6149.
- Faustini, M.; Nicole, L.; Boissiere, C.; Innocenzi, P.; Sanchez, C.; Grosso, D. *Chem. Mater.* **2010**, *22*, 4406–4413.
- Hrubesh, L. W.; Pekala, R. W. *J. Mater. Res.* **1994**, *9*, 731–738.
- Yoldas, B. E.; Annen, M. J.; Bostaph, J. *Chem. Mater.* **2000**, *12*, 2475–2484.
- Li, L.; Yalcin, B.; Nguyen, B. N.; Meador, M. A. B.; Cakmak, M. *ACS Appl. Mater. Interfaces* **2009**, *1*, 2491–2501.
- Beck, J. S.; Vartuli, J. C.; Roth, W. J.; Leonowicz, M. E.; Kresge, C. T.; Schmitt, K. D.; Chu, C. T. W.; Olson, D. H.; Sheppard, E. W.;

- Mccullen, S. B.; Higgins, J. B.; Schlenker, J. L. *J. Am. Chem. Soc.* **1992**, *114*, 10834–10843.
- (13) Zhao, D. Y.; Feng, J. L.; Huo, Q. S.; Melosh, N.; Fredrickson, G. H.; Chmelka, B. F.; Stucky, G. D. *Science* **1998**, *279*, 548–552.
- (14) Lu, Y. F.; Ganguli, R.; Drewien, C. A.; Anderson, M. T.; Brinker, C. J.; Gong, Y. X.; Soyez, H.; Dunn, B.; Huang, M. H.; Zink, J. I. *Nature* **1997**, *389*, 364–368.
- (15) Gorman, B. P.; Orozco-Teran, R. A.; Roepsch, J. A.; Dong, H.; Reidy, R. F. *Appl. Phys. Lett.* **2001**, *79*, 4010–4012.
- (16) Leventis, N.; Sotiriou-Leventis, C.; Zhang, G. H.; Rawashdeh, A.-M. M. *Nano Lett.* **2002**, *2*, 957–960.
- (17) Xia, Z.; Riester, L.; Sheldon, B. W.; Curtin, W. A.; Liang, J.; Yin, A.; Xu, J. M. *Rev. Adv. Mater. Sci.* **2004**, *6*, 131–139.
- (18) Miyoshi, H.; Hata, N.; Kikkawa, T. *Jpn. J. Appl. Phys.* **2005**, *44*, 1166–1168.
- (19) Gaire, C.; Ou, Y.; Arao, H.; Egami, M.; Nakashima, A.; Picu, R. C.; Wang, G.-C.; Lu, T.-M. *J. Porous Mater.* **2010**, *17*, 11–18.
- (20) Cha, B. J.; Kim, S.; Char, K.; Lee, J.-K.; Yoon, D. Y.; Rhee, H.-W. *Chem. Mater.* **2006**, *18*, 378–385.
- (21) Sing, K. S. W.; Everett, D. H.; Haul, R. A. W.; Moscou, L.; Pierotti, R. A.; Rouquérol, J.; Siemieniewska, T. *Pure Appl. Chem.* **1985**, *57*, 603–619.
- (22) Brinker, C. J.; Scherer, G. W. *Sol-Gel Science, The Physics and Chemistry of Sol-Gel Processing*; Academic Press: New York, 1990.
- (23) Tilgner, I. C.; Fischer, P.; Bohnen, F. M.; Rehage, H.; Maier, W. F. *Micropor. Mater.* **1995**, *5*, 77–90.
- (24) Lee, D. W.; Yu, C. Y.; Lee, K. H. *J. Phys. Chem. C* **2008**, *112*, 5136–5140.
- (25) Brinker, C. J.; Sehgal, R.; Hietala, S. L.; Deshpande, R.; Smith, D. M.; Loy, D.; Ashley, C. S. *J. Membr. Sci.* **1994**, *94*, 85–102.
- (26) Nair, B. N.; Elferink, W. J.; Keizer, K.; Verweij, H. *J. Colloid Interface Sci.* **1996**, *178*, 565–570.
- (27) Elferink, J. W.; Nair, B. N.; de Vos, R. M.; Keizer, K.; Verweij, H. *J. Colloid Interface Sci.* **1996**, *180*, 127–134.
- (28) Nair, B. N.; Elferink, J. W.; Keizer, K.; Verweij, H. *J. Sol-Gel Sci. Technol.* **1997**, *8*, 471–475.
- (29) Schaefer, D. W. *Science* **1989**, *24*, 1023–1027.
- (30) Raman, N. K.; Anderson, M. T.; Brinker, C. J. *Chem. Mater.* **1996**, *8*, 1682–1701.
- (31) Shimizu, W.; Murakami, Y. *ACS Appl. Mater. Interfaces* **2010**, *2*, 3128–3133.
- (32) Chu, L.; Tejedor-Tejedor, M. I.; Anderson, M. A. *Microporous Mater.* **1997**, *8*, 207–213.
- (33) Meixner, D. L.; Gilicinski, A. G.; Dyer, P. N. *Langmuir* **1998**, *14*, 3202–3209.
- (34) Colomer, M. T.; Anderson, M. A. *J. Non-Cryst. Solids* **2001**, *290*, 93–104.
- (35) Kremer, S. P. B.; Kirschhock, C. E. A.; Tielen, M.; Collignon, F.; Grobet, P. J.; Jacobs, P. A.; Martens, J. A. *Adv. Funct. Mater.* **2002**, *12*, 286–292.
- (36) Groen, J. C.; Peffer, L. A. A.; Pérez-Ramírez, J. *Microporous Mesoporous Mater.* **2003**, *60*, 1–17.
- (37) Endo, A.; Miyata, T.; Akiya, T.; Nakaiwa, M.; Inagi, Y.; Nagamine, S. *J. Mater. Sci.* **2004**, *39*, 1117–1119.
- (38) Di, Y.; Meng, X.; Wang, L.; Li, S.; Xiao, F.-S. *Langmuir* **2006**, *22*, 3068–3072.
- (39) Shimizu, W.; Matsumoto, T.; Hosoo, S.; Nagahira, H.; Murakami, Y. *J. Ceram. Soc. Jpn.* **2007**, *115*, 712–716.
- (40) Orthaber, D.; Bergmann, A.; Glatter, O. *J. Appl. Crystallogr.* **2000**, *33*, 218–225.
- (41) Glatter, O. *J. Appl. Crystallogr.* **1977**, *10*, 415–421.
- (42) Glatter, O. *Acta Phys. Austriaca* **1977**, *47*, 83–102.
- (43) deBoer, J. H.; Linsen, B. G.; van der Plas, T.; Zondervan, G. J. *J. Catal.* **1965**, *4*, 649.
- (44) Boury, B.; Corriu, R. J. P.; Strat, V. L. *Chem. Mater.* **1999**, *11*, 2796–2803.
- (45) Colomer, M. T.; Anderson, M. A. *J. Non-Cryst. Solids* **2001**, *290*, 93–104.
- (46) Brunaure, S.; Emmett, P. H.; Teller, E. *J. Am. Chem. Soc.* **1938**, *60*, 309.
- (47) Barrett, E. P.; Joyner, L. G.; Halenda, P. P. *J. Am. Chem. Soc.* **1951**, *73*, 373.
- (48) Horváth, G.; Kawazoe, K. *J. Chem. Eng. Jpn.* **1983**, *16*, 470–475.
- (49) Saito, A.; Foley, H. C. *AIChE J.* **1991**, *37*, 429–436.
- (50) Glatter, O.; Kratky, O. *Small-Angle X-Ray Scattering*; Academic Press: London, 1982.
- (51) Ornstein, L. S.; Zernike, F. *Proc. Acad. Sci. Amsterdam* **1914**, *17*, 793–806.
- (52) Debye, P. *J. Phys. Colloid Chem.* **1947**, *51*, 18–32.
- (53) Pedersen, J. S.; Schurtenberger, P. *Macromolecules* **1996**, *29*, 7602–7612.
- (54) Pedersen, J. S.; Schurtenberger, P. *J. Polym. Sci., Part B: Polym. Phys.* **2004**, *42*, 3081–3094.
- (55) Strobl, G. R. *The Physics of Polymers: Concepts for Understanding Their Structures and Behavior*, 3rd ed.; Springer: Berlin, 2007.
- (56) Toporowski, P. M.; Roovers, J. E. L. *Macromolecules* **1978**, *11*, 365–368.
- (57) Brian M. Tande, B. M.; Wagner, N. J.; Mackay, M. E.; Hawker, C. J.; Jeong, M. *Macromolecules* **2001**, *34*, 8580–8585.
- (58) Fukasawa, T.; Sato, T. *Phys. Chem. Chem. Phys.* **2011**, *13*, 3187–3196.
- (59) Sato, T.; Komatsu, T.; Nakagawa, A.; Tsuchida, E. *Phys. Rev. Lett.* **2007**, *98*, 208101.
- (60) Pouxviel, J. C.; Boilot, J. P. *J. Non-Cryst. Solids* **1987**, *94*, 374.
- (61) Sanchez, J.; McCormick, A. *J. Phys. Chem.* **1992**, *96*, 8973–8979.
- (62) Mazur, M.; Mlynarik, V.; Valko, M.; Pelican, P. *Appl. Magn. Reson.* **1999**, *16*, 547–557.
- (63) Boury, B.; Corriu, R. J. P.; Strat, V. L. *Chem. Mater.* **1999**, *11*, 2796–2803.
- (64) Groen, J. C.; Peffer, L. A. A.; Pérez-Ramírez, J. *Microporous Mesoporous Mater.* **2003**, *60*, 1–17.